

# Electron backscatter diffraction postprocessing techniques for studying recrystallisation phenomenon of Ferritic Stainless Steel

Muhammed Y. Salojee<sup>1</sup>, Charles W. Siyasiya<sup>1</sup>, Kofi A. Annan<sup>1,2</sup>, and Joseph Moema<sup>3</sup>

<sup>1</sup>Department of Material Science and Metallurgical Engineering, University of Pretoria, South Africa.

<sup>2</sup>Metallurgical Engineering Services, Regional Operations & Asset Services, Sasol Synfuels, Secunda.

<sup>3</sup>Advanced Materials Division (AMD), Mintek, South Africa.

**Abstract.** The following article looks at using scanning electron microscopy- electron back scatter diffraction techniques to study recrystallisation structures produced through hot rolling of 436 ferritic stainless steel. Characterisation of recrystallisation textures was undertaken through analysis of misorientation angle distribution diagrams, orientation distribution function maps, inverse pole figures and Taylor factor maps. These techniques were applied in a case study where typical industrial hot rolling conditions were simulated through uniaxial compression tests in a Bähr Dilatometer 850D, whereby the effect of strain rate and interpass time on recrystallisation structures was investigated.

## 1 Introduction

Ferritic Stainless Steels (FSS) have proven their financial stability over austenitic stainless steels (ASS) after nickel prices soared between March and April of 2022. The mechanical and corrosion properties of FSS are comparable to ASS and therefore offer an attractive alternative to ASS. The 436 FSS has Cr, Nb and Mo additions, to stabilise the ferritic structure at all temperature ranges and improve corrosion resistance. It is used in the visible parts of exhaust systems and automotive trimming [1].

The downside of FSS is the plastic anisotropy which many authors attribute to the clustering of preferred orientations during processing [1-4]. The cumulation of preferred grain orientations is a result of both the casting and rolling processes, coupled with the stacking fault energy of body-centred cubic (BCC) crystals. The casting process allows for the preferential growth of columnar grains with cube texture  $\{001\} \langle 010 \rangle$ , which are inherently difficult to deform and recrystallise. This prevent the randomisation of grain orientations [4]. The high stacking fault energy of BCC crystals allows for cross slip during high temperature deformation and subsequent recovery as opposed to recrystallisation. During cold drawing of FSS sheets, anisotropy manifests as corrugations on the sheet surface called ridges which require large amounts of polishing and grinding to remove. These ridges take away from the sheet's aesthetics and is of foremost importance in application [5, 6].

As mentioned, processing contributes to accumulation of preferred orientations. Therefore, controlling these process parameters during hot rolling can minimise and reduce the effects of textural clustering in the final sheet product. Electron backscatter diffraction

(EBSD) is a functional tool to study the effects of crystal orientation in processing of sheet products. Characterisation through EBSD can provide and improve insight into optimising the recrystallisation behaviour of FSS [5, 6].

## 2 Methodology

Cylindrical samples of 436 FSS with dimensions of 5 mm diameter with 10 mm length were machined and subjected to uniaxial isothermal hot compression tests in four passes using the Bähr 850D Dilatometer. Strain rates and interpass times were varied in order to characterise the recrystallisation under various conditions. A series of four tests were carried out as stipulated in Table 1. Aside from strain rates, temperature and strain parameters were aligned to typical hot rolling conditions as shown by Kodukula and Annan [8, 13].

**Table 1.** Test matrix for deformation schedule used.

Parameter		Roughing				
		P1	P2	P3	P4	
Strain rate	Temperature (°C)	1000	960	930	900	
	Strain	0.24	0.3	0.23	0.23	
5/s	Interpass time (s)	Short	20	20	20	20
		Long	40	40	40	40
15/s	Interpass time (s)	Short	20	20	20	20
		Long	40	40	40	40

Following deformation tests, samples were sectioned midway along the deformation axis and analysed through EBSD analysis. EBSD acquisition was conducted by use of a Jeol scanning electron microscope (SEM) IT300LV fitted with a Nordys Nano for EBSD analysis and XMAX<sup>N</sup> for Energy Dispersive Spectroscopy (EDS). The sectioned samples had a cross section as shown in Figure 1. The normal direction (ND) is parallel to the deformation/compression axis, the rolling direction (RD) is parallel to the direction of plastic flow and the transverse direction (TD) is perpendicular to these directions. The AZtec Channel 5, HKL software was used to process EBSD results. A variety of step sizes, were used in order to evaluate recrystallisation structures present. Voltage was maintained at 20 V, working distances at 20 mm and incline angles at 70°. Grain boundaries were depicted from 3° and high angle grain boundaries at 15°, unless stated otherwise.

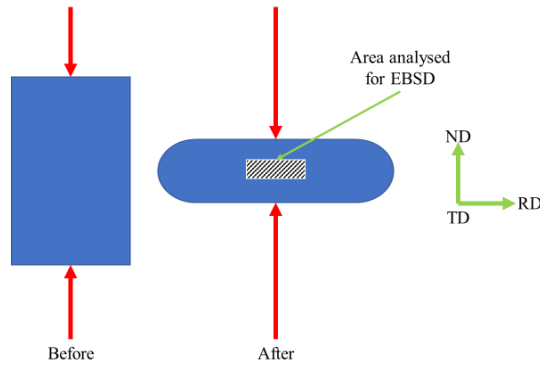


**Fig. 1.** Cross sections of the cylindrical test pieces, before and disc like specimen, after uniaxial compression tests, with the hatch area depicting where samples were analysed for EBSD.

### 3 Results and Discussions

In Figure 2a, the overall area is dominated by a cube texture, whilst Figure 2b shows the Inverse Pole Figure (IPF) at high magnification drawn along the RD direction, with the corresponding Orientation Distribution Function (ODF) image. The close-up image of the area recrystallised (Figure 2b) within the cube grain shows that the recrystallised grains have a  $\gamma$ -fibre texture circled in red on the ODF image [2, 3]. The lowered intensity around the cube orientation moving from an intensity of 25.8 to an intensity of 23.9 is evident that the recrystallised grains shown in Figure 2b are breaking down the cube texture and forming a  $\gamma$ -fibre texture. The IPF image used in conjunction with the ODF map provided a more descriptive analysis of the recrystallised structure than using a single tool alone.

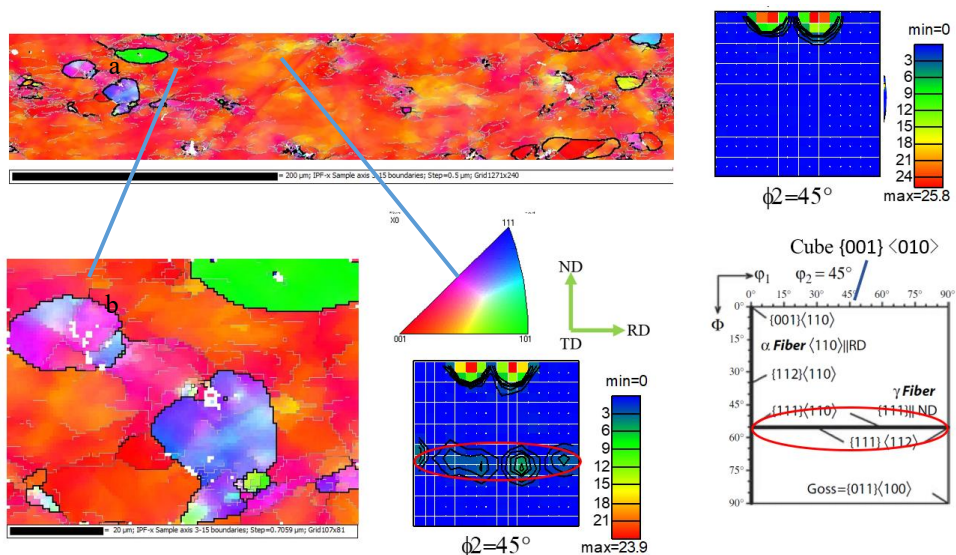


**Fig. 2.** IPF image of, a sample deformed at long interpass times and high strain rates; (a) top, IPF image drawn relative to RD (step size 0.5  $\mu\text{m}$ ) for large area analysis, right, corresponding ODF image, (b) bottom, close up of IPF area (step size 0.7  $\mu\text{m}$ ) in a with corresponding ODF section, showing presence of  $\gamma$ -fibre presence. ODF reference on bottom right corner, adapted from Engler and Randle [2].

EBSD mapping can be processed to create texture maps. In this study, textural maps were created for the important textures in BCC materials, namely, Cube ( $\{001\} \langle 100 \rangle$ ), Copper ( $\{112\} \langle 111 \rangle$ ), Goss ( $\{011\} \langle 100 \rangle$ ), S ( $\{123\} \langle 634 \rangle$ ) and Brass ( $\{011\} \langle 211 \rangle$ ) textures [2]. The processing of these maps is done by taking the ideal texture orientation and checking for textures that deviate from the ideal within  $20^\circ$ . In this document, Cube textures are depicted in blue, Copper in pink, Goss in red, S in green and Brass in yellow. Figure 3a shows that recrystallised grains from the parent cube texture, either do not belong to a specific textural component (coloured in white) or belong to S or copper textures (coloured in green and pink). This is consistent with work published by Doherty et al. [10] where Particle stimulated nucleation (PSN) is reported to randomise the texture.

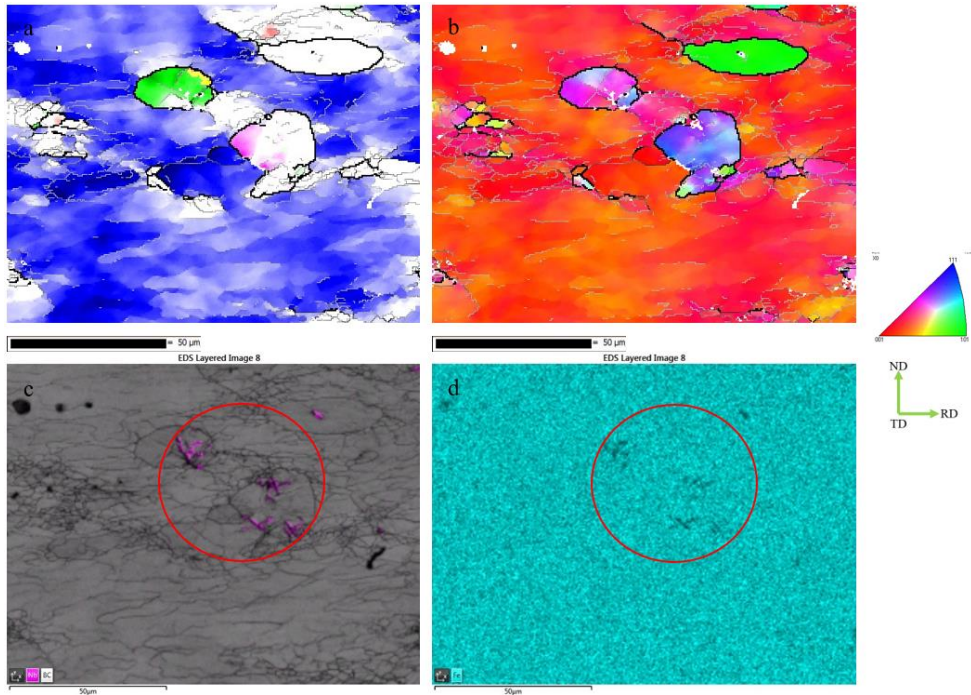


**Fig. 3.** Close up to area analysed along ND-RD plane in Figure 2: (a) depicts a textural map, (b) an IPF image relative to the RD, (c) an EDS Nb map layered with a band contrast image to show the distribution of grain boundaries around the precipitates and (d) depicts an Fe map to show the presence of Fe in the sample with depletion at precipitates. Step size  $0.5 \mu\text{m}$ .

Considering that the recrystallised grains seem to be concentrated in a certain portion of the image in Figure 3, questions may arise as to why these areas are prone to recrystallise and others are not. A useful tool that can be coupled with EBSD analysis is EDS mapping. It is noted that recrystallised grains are concentrated around precipitates. These precipitates are rich in Nb and depleted in Fe as shown in Figure 3c and 3d. This analysis indicates that recrystallisation is driven by PSN, where intensely and heterogeneously deformed regions around precipitates act as nucleation sites for recrystallisation [10]. In other words, integrating texture, IPF and EDS mapping provides a clear picture of the dynamics involved in recrystallisation encouraged by PSN.

The recrystallisation fraction map in Figure 4 classifies grains as either deformed (in red), recrystallised (in blue) or substructure (yellow). The software defines these grains by firstly reconstructing grains, measuring the internal misorientation of each reconstruct grain and

classifying it into the one of the three mentioned categories. The software is useful in determining statically recrystallised grains in blue. In this case we are likely to find recrystallisation in the form of dynamic recrystallisation. These maps are still useful in that newly formed dynamically recrystallised grains would have low dislocation density due to the recrystallisation process. Furthermore, it is seen that adjacent to highly deformed red grains, we find blue grains showing a transition to a lower strained structure.

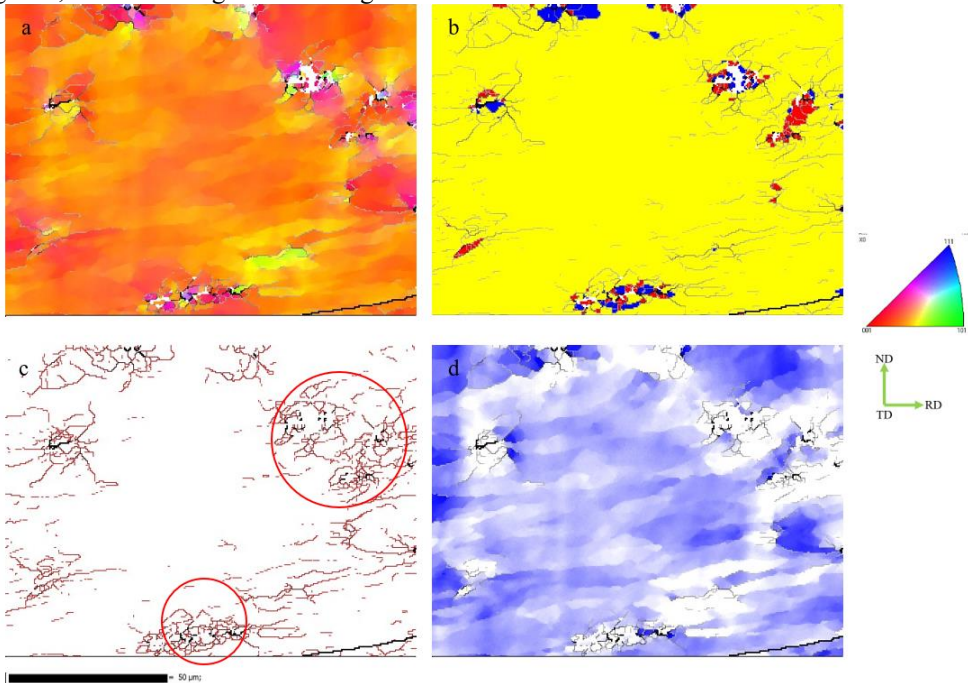


**Fig. 4.** EBSD images of a sample deformed at shorter interpass times and high strain rates: (a) depicts an IPF map drawn relative to the RD, (b) a recrystallisation fraction map, (c) a grain boundary map and (d) a texture map. Step size 0.45  $\mu\text{m}$ .

Lowering interpass times, shows a decrease in the size and extent of recrystallised grains, typical of previous studies [10, 11]. This is evident in Figure 4 where the sample was deformed at shorter interpass times but at high strain rates. Note, the texture map still shows cube texture of the parent grain, however, recrystallised grains do not hold any specific textural orientation and can be said to be random, consistent with previous work [9]. Included in these maps is a grain boundary map and recrystallisation fraction map. The grain boundary map depicts boundaries where areas in the map have a misorientation above a certain degree, in this case, sub-grains having orientations between  $2^\circ$  and  $15^\circ$  are depicted in red, whilst high angle boundaries with misorientation greater than  $15^\circ$  are depicted in black. By looking at Figure 4c and Figure 5 in conjunction, it is noted that precipitates are surrounded by high angle boundaries and transform into low angle grain boundaries when moving away from the precipitate typical of PSN. These areas are circled in red on both figures. Continuous dynamic recrystallisation (CDRX) can occur through accumulation of dislocations into low angle grain boundaries and subsequently into high angle grain boundaries [12]. Considering the formation of high angle grain boundaries around precipitates with low angle grain boundaries away from precipitates, the PSN, could be said to assist Dynamic recrystallisation (DRX), this eludes to the possibility of CDRX through PSN which has not been evidenced before. Further work would need to be done to confirm if DRX is occurring through CRX. De

Siqueira [13], found the minimum size of precipitates for PSN to occur in Nb-FSS as  $1\mu\text{m}$ . The precipitates in this study are larger and thus PSN is expected.

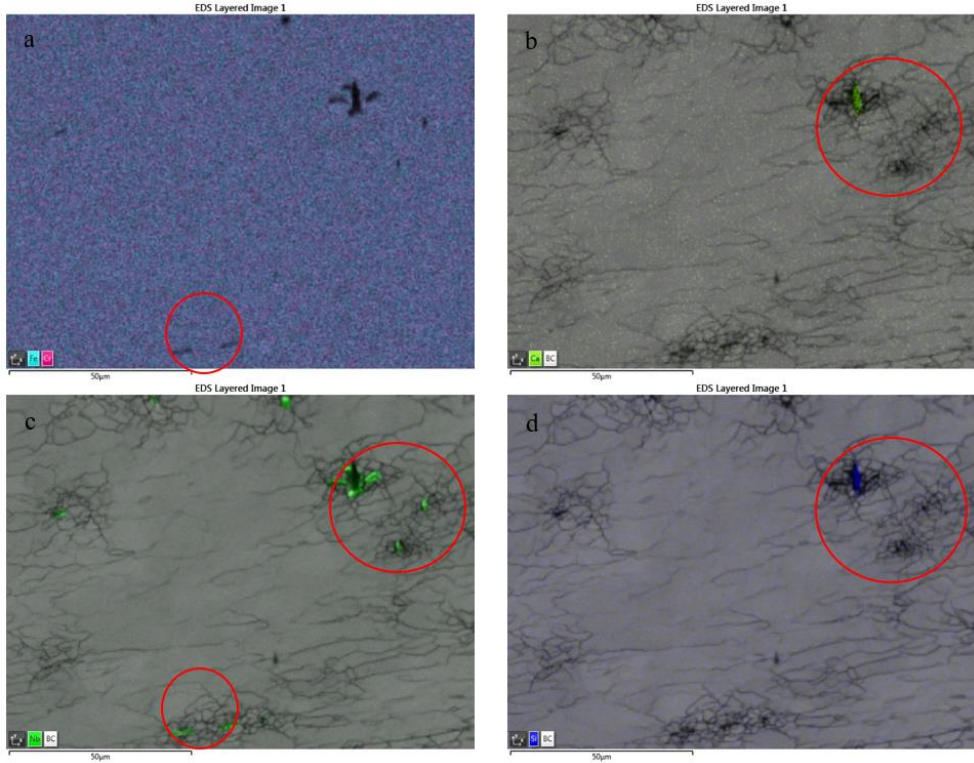


**Fig. 5.** EDS maps of a sample deformed at shorter interpass times and high strain rates: (a) depicts a Cr-Fe map, b, c and d are band contrast maps layered with Ca, Nb and Si respectively.

By consolidating EBSD maps in Figure 4 with EDS maps in Figure 5, we find that the star-shaped precipitates formed are depleted in Cr and Fe, being characterised by high Nb concentration. Also shown is an area characterised by Si and Ca, characteristic of inclusions in the top right of the image. It is worthwhile to note that the largest Nb-rich precipitates formed heterogeneously around inclusions, [14].

EBSM images of the sample deformed at longer interpass times and lowered strain rates is depicted in Figure 6. Of interest here is Figure 6d, which shows a Taylor Factor (TF) map. TF maps are drawn on a colour scale where high TF grains are depicted in red, while low TF grains are depicted in blue. The Taylor factor defines the amount of work required to deform grains to the same strain plastically. The higher the TF the more likely a grain is to favour recovery at high temperatures [3, 17]. Proof of this is the grain, arrowed in blue, shows minimal low angle grain boundaries relative to other grains depicted. Note on comparison that deformation structures with higher interpass times show larger recrystallised grains. By integrating TF analysis, studies into why strains accumulate in specific grains above others can be undertaken and better understood.

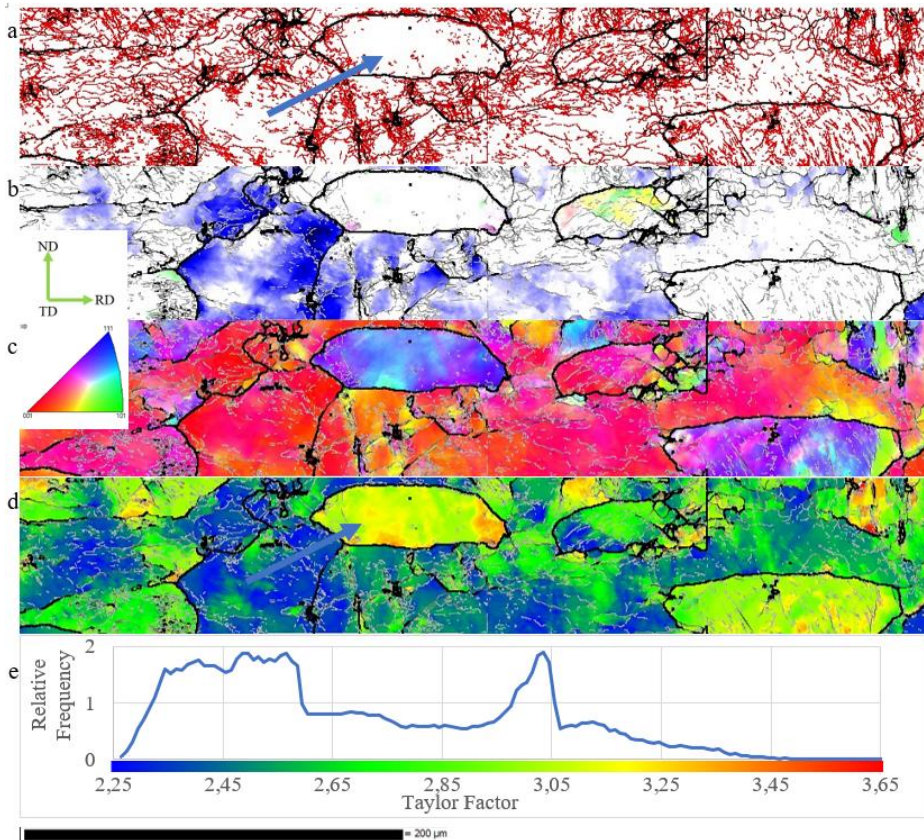


**Fig. 6.** EBSD images taken on the ND-RD plane of a sample deformed at longer interpass times and lower strain rates: (a) depicts a grain boundary map, (b) a texture map, (c) an IPF map relative to the RD, (d) a Taylor Factor map drawn relative to the RD and (e) Taylor factor intensity distribution for d. Step size 0.5  $\mu\text{m}$ .

Both correlated and uncorrelated Misorientation Angle Distribution (MAD) diagrams are plotted in Figure 7. Misorientation data summarises the relative change in misorientation between various pixels in the image. It is known that high angle grain boundaries have misorientations greater than  $10\text{-}15^\circ$  and low angle grain boundaries have misorientations greater than  $5^\circ$ . Misorientations less than  $5^\circ$  can be seen as sub structure. In this way an understanding of the general misorientations between and within grains can be explored as a cast, undeformed structure would be characterised by high angle grain boundaries.

Work by Humphrey [18] shows that plotting of correlated data is far more precise relative to uncorrelated data as uncorrelated data may produce numerous false boundaries in a structure. This is due to correlated data having the ability to identify changes in orientations that result in grain boundaries between neighbouring pixels, but with uncorrelated data is taken from random pixels in the structure. Considering the uncorrelated data for the samples analysed (Figure 7a), orientations of recrystallised grains do not differ much from the parent grain in that MAD misorientations are concentrated at lower misorientation angles. As the larger proportion of the areas analysed constitutes the parent grain, from the random points indexed relative to each other, the proportion of which will be the parent grain will likely be high. This means that the misorientation of the uncorrelated data is concentrated at lower intensity, the difference in orientation of recrystallised grains formed would not differ much from that of the parent grain. It is worthwhile noting that grain misorientations peak at less

than  $10^0$ , which indicates that a large majority of new grains are formed through DRX as grains are formed through recovery of dislocations into low angle grain boundaries [12]. The presence of low angle grain boundaries is not usually found in the cast, as shown by Modak [5], therefore the formation of low angle grain boundaries is through the mechanism of CDRX. Longer interpass times show a greater degree of high angle grain boundary intensity relative to shorter interpass times correlating to work by numerous authors [11, 18].

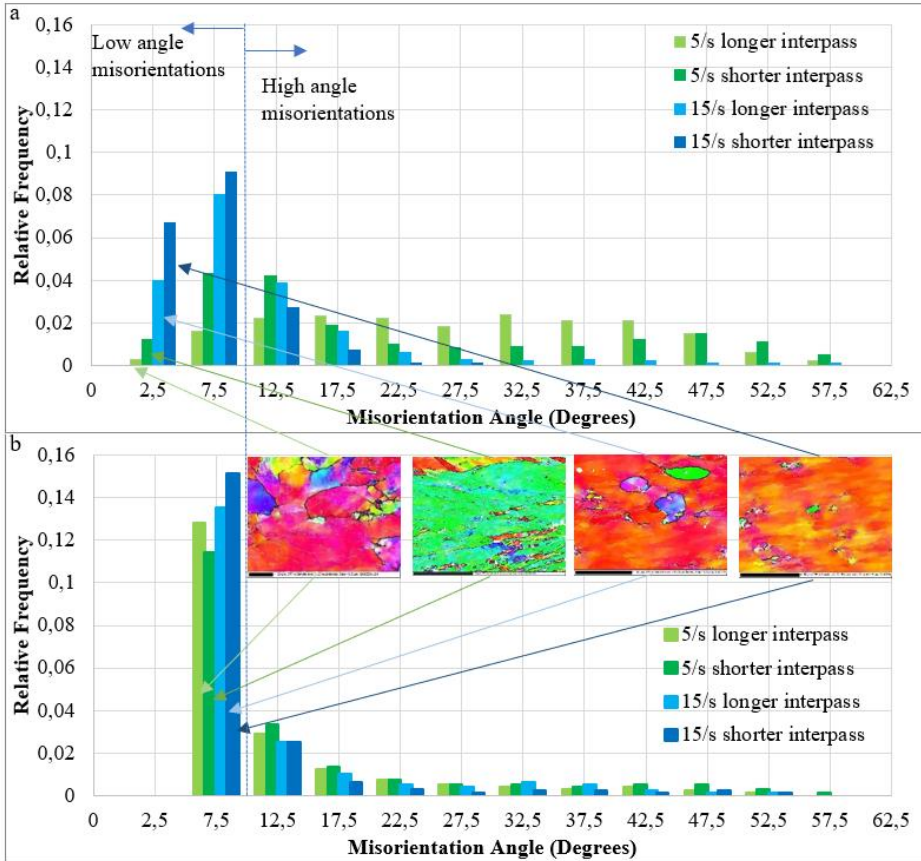


**Fig. 7.** Misorientation angle distributions (MAD) of mapped areas for all samples analysed: (a) uncorrelated, misorientation between two randomly selected pixels, (b) correlated, misorientation between neighbouring pixels.

The correlated misorientation angle distribution diagrams illustrate that newly formed, recrystallised grains have a greater degree of misorientation relative to the parent grain with the misorientation being more pronounced in grains strained at lower strain rates. A wide variety of grain misorientations are formed during low strain rates with higher strain rates being typical of a material with a large degree of low angle grain boundary presence. Higher interpass times are found to shift the misorientation profiles of recrystallised grains to higher angles of misorientation. It can thus be said that longer interpass times favours high angle grain boundaries through static recrystallisation, whilst low strain rates favour CDRX.

## 4 Conclusions

When EBSD processing and EDS techniques are used to complement each other, much more insight is brought into recrystallisation phenomenon. By using these techniques on a hot

rolling case study to evaluate the effect of strain rate and interpass time on the recrystallisation behaviour, it was found that:

- Recrystallisation in the 436 system is possible and assisted by PSN in the material. This is due to inclusions and precipitates that act as nucleation sites due to intense deformation around them.
- Recrystallisation through PSN was found to randomise and breakdown the cast Cube texture.
- Recrystallisation was concentrated around inclusions and precipitates, and this implied that by encouraging a large volume fraction of homogeneously distributed precipitates, it can likely promote the recrystallisation process and the breaking down of the undesirable Cube texture.
- Longer interpass times and slower strain rates allow for recrystallization while higher strain rates and shorter interpass time allow for the formation of the substructure.
- Generally, not a lot of information can be generated from IPF maps, however, when combined with ODF cross sections it provides a clear understanding of the overall texture and gives a clear idea of changes in the texture when areas of interest are chosen.
- Texture maps provide a convenient tool to highlighting textures of interest, without the need of ODF cross sections.
- Coupling of EDS with EBSD analysis can give explanations of material behaviour to understand local deformation behaviour around secondary phase particles typical of PSN.
- MAD data provides insights into the presence of high angle and low angle grain boundaries present as well as the presence of substructure. In recrystallisation mechanisms where recrystallised grains move from low angle misorientations to high angle misorientations, MAD provides useful information to support such insights.

## Acknowledgements

The authors would like to acknowledge, Columbus Stainless Pty Ltd and DSI-Mintek for the financial and technical support, and the University of Pretoria for the research facilities.

## References

1. J. Fu, K. Cui, F. Li, J. Wang and Y. Wu, *Matls Charac*, **159**, 1-11, (2020).
2. O. Engler and V. Randle, *Introduction to Texture Analysis: Macrotecture, Microtexture and Orientation Mapping*, (2010).
3. L. A. I. Kestens and H. Pirgazi, *Matl Science Tech.*, **32**, no. 13, 1303-1315, (2016).
4. K. Yvell, *Experimental Studies of Deformation Structures in Stainless Steels using EBSD*, (2018).
5. P. Modak, S. Patra, R. Mitra & D. Chakrabarti, *Metal. & Matls. Trans. A*, **49**, p. 2219-2234, (2018).
6. D. Raabe, *Matls Science Eng A*, **197**, 31-37, (1995).
7. R. A. Swarzer and J. Sukkau, *Banaras Metallurgist*, **18**, 1-11, (2013).

8. S. Kodukula, H. Kokkomäki E. Puukko, D. Porter and J. Kömi, *Steel Research Intl.*, **92**, no. 7, (2021)
9. B. Roebuck, J. Lord, M. Brooks, M. Loveday, C. Sellars and R. Evans, *Matls High Temp*, **23**, no. 2, 59–83, (2006).
10. R. D. Doherty, D. A. Hughes, F. J. Humphreys, J. J. Jonas, D. J. Jensen, M. E. Kassner and W. E. King, *Matls Science and Eng*, **238**, A, 219, (1997).
11. F. V. Braga, D. M. P. Escobar, N. J. L. d. Oliveira and M. S. Andrade, *J. of Matls Research*, **1**, no. 5, (2016).
12. K. Huang, R. E. Loge, *Matls Design*, **111**, (2016).
13. K. Annan, C. Siyasiya and W. Stumpf, *J SAIMM*, **113**, no. 2, (2013).
14. R. P. de Siqueira, H. R. Z. Sandim, D. Raabe, *Metal Matls Trans A*, **44**, no. A, 469-478, (2013).
15. M. P. Sello, *The laves phase embrittlement of ferritic stainless steel type AISI 441*, (2009).
16. J. W. Matthews and a. F. R. N. Nabarro, *Amsterdam*, 463, (1979).
17. G. J. Shiflet, *Matls Science Eng*, **81**, 61-100, (1986).
18. J. Jiang, T. B. Britton and A. J. Wilkinson, *International Journal of Plasticity*, vol. **69**, 102–117, (2015).
19. K. Annan, *Effect of hot working characteristics on the texture development in AISI 430 and 433 ferritic stainless steel*, Pretoria (2012).
20. F. J. Humphreys, *Journal Microscopy*, **213**, no. 3, 247–256, (2004).
21. S. Kodukula, H. Kokkomäki, E. Puukko, D. Porter and J. Kömi, *Steel Research Internl*, **92**, no. 7, (2021).
22. J. E. Nye, *Acta Mater.* **1**, 153-162, (1953).
23. G. He, L. Tan, F. Liu, L. Huang and Z. H. a. L. Jiang, *Materials* **10** (161), 1-14, (2017).
24. B. Dutta, E. J. Palmiere and C. M. Sellars, *Acta Materialia*, **49**, no. 5, 785-794, (2001).
25. T. Konkova, S. Mironov, A. Korznikov, G. Korznikova, M. M. Myshlyayev and S. Semiatin, *Mats Charac*, **101**, 173–179, (2015).
26. P. J. Konijnenberg, S. Zaefferer and D. Raabe, *Acta Materialia*, **99**, 402–414, (2015)